Materials Horizons

ROYAL SOCIETY OF CHEMISTRY

COMMUNICATION

View Article Online
View Journal

Check for updates

Cite this: DOI: 10.1039/d5mh01682g

Received 3rd September 2025,
Accepted 8th December 2025

DOI: 10.1039/d5mh01682g

rsc.li/materials-horizons

Metabolic-switch macrophage cyborgs reverse atherosclerosis by photoacoustic-directed on-demand phenotype delivery

Wei Zeng,†[a] Weimin Fang,†[ab] Yuhang Mao,†[c] Yalan Huang,†[ab] Yan Lin,[d] Leilei Wu,[e] Anqi Chen,[f] Zhengan Huang,[f] Yuanyuan Sheng,[a] Xiaoxuan Lin,[a] Jiayu Ye,[a] Yanbin Guo,[a] Guanxi Wen,[a] Jian Zeng,[e] Jinfeng Xu, *[a] Liqiang Zhou *[gh] and Yingying Liu *[a]

Pathological macrophage activation orchestrates atherosclerotic plaque progression through sustained inflammation, necrotic core expansion, and plaque destabilization, a process recalcitrant to current targeted therapies. We address this fundamental challenge by engineering a living macrophage-based theranostic cyborg (MφMB-Au) that integrates precision plaque homing with spatiotemporally controlled immunomodulation. This platform exploits the innate inflammatory tropism of functionalized macrophages to co-deliver gold nano-regulator (AuNPs) and real-time tracer microbubbles (MBs). The AuNPs function dually as high-sensitivity photoacoustic imaging agents, enabling deep-tissue quantification of plaque burden, and potent metabolic switches reprogramming macrophage polarization *via* lipid and energy metabolism pathways. Concurrently, MBs facilitate real-time ultrasonographic tracking with micron-scale spatial resolution. *In vivo* studies demonstrate sustained plaque-specific accumulation of MφMB-Au, permitting longitudinal dual-modal ultrasound/photoacoustic imaging for over 24 hours. Ultrasound-triggered payload release induced a 5.3-fold increment of M2-repolarization, driving significant plaque regression. Critically, this approach restored efferocytosis capacity and collagen deposition while evading off-target toxicity. As the first cellular cyborg platform unifying longitudinal multimodal imaging, stimuli-responsive cargo deployment, and metabolic reprogramming, this work establishes a paradigm-shifting theranostic strategy to reverse the core pathophysiology of atherosclerosis.

New concepts

This study introduces a novel "macrophage cyborg" system (MφMB-Au) that represents a groundbreaking theranostic approach for atherosclerosis. By integrating living macrophages with gold nanoparticle-loaded microbubbles, the platform achieves targeted delivery to inflammatory plaques through innate cellular homing, while enabling real-time, dual-modality ultrasound and photoacoustic imaging for precise tracking over 24 hours. Its uniqueness lies in the synergistic combination of metabolic reprogramming and spatiotemporally controlled phenotype switching: upon ultrasound-triggered release, the gold nanoparticles potently polarize macrophages toward an anti-inflammatory M2 state *via* modulation of lipid and energy metabolism pathways. This not only reverses plaque progression and enhances stability by restoring efferocytosis and collagen deposition but also systemically modulates immune cells, elevating regulatory T cells and reducing pro-inflammatory subsets. The innovation encompasses a living-cell vector that unites longitudinal imaging, stimulus-responsive drug release, and metabolic immunotherapy, offering a targeted and biocompatible strategy to counteract atherosclerosis at its inflammatory core.

1. Introduction

Atherosclerosis (AS), a chronic inflammatory vascular disease, is estimated to account for 85% of annual cardiovascular disease mortality rates.[1] Inflammation underlies every stage of AS-from initiation and progression to the onset of clinical

[a] Department of Ultrasonography, Shenzhen People's Hospital (The First Affiliated Hospital, Southern University of Science and Technology; The Second Clinical Medical College, Jinan University), Shenzhen 518020, China. E-mail: jinfengxu@ext.jnu.edu.cn, yingyingliu@ext.jnu.edu.cn
[b] Post-doctoral Scientific Research Station of Basic Medicine, Jinan University, Guangzhou 510632, China
[c] School of Medicine, Ankang University, Ankang 725000, China
[d] Department of Plastic Surgery, Renmin Hospital of Wuhan University, Wuhan 430060, China
[e] Department of Thoracic Surgery, Zhejiang Cancer Hospital, Hangzhou Institute of Medicine (HIM), Chinese Academy of Sciences, Hangzhou 310004, P. R. China
[f] Guangdong Cardiovascular Institute, Guangdong Provincial People's Hospital (Guangdong Academy of Medical Sciences), Southern Medical University, Guangzhou 519041, China
[g] Faculty of Health Sciences, University of Macau, Macau, SAR 999078, P. R. China. E-mail: liqiangzhou@um.edu.mo
[h] MoE Frontiers Science Center for Precision Oncology, University of Macau, Macau, SAR 999078, P. R. China
† Wei Zeng, Weimin Fang, Yuhang Mao and Yalan Huang contributed equally to this work.

Open Access Article. Published on 23 December 2025. Downloaded on 1/24/2026 10:53:48 PM. This article is licensed under a Creative Commons Attribution-NonCommercial 3.0 Unported Licence.

Open Access Article. Published on 23 December 2025. Downloaded on 1/24/2026 10:53:48 PM. This article is licensed under a Creative Commons Attribution-NonCommercial 3.0 Unported Licence.

complications.[2] The gradual expansion of atherosclerotic plaques or the sudden rupture of vulnerable lesions can trigger life-threatening events, such as acute myocardial infarction, stroke, or unexpected cardiac arrest.[3,4] Hence, early monitoring and treatment of AS is crucial for alleviating its progression and reducing mortality rates. The current non-surgical treatment of atherosclerosis primarily focuses on lipid-lowering therapies,[5] anti-inflammatory strategies,[6] and lifestyle interventions.[7] Surgical interventions mainly include percutaneous coronary intervention, coronary artery bypass grafting,[8] and carotid endarterectomy.[9] However, the incidence and mortality rates of cardiovascular events caused by plaque rupture remain extremely high. Consequently, exploring new therapeutic avenues for AS management is of paramount importance.

Macrophages (Mφ) act as key regulators of chronic inflammation and are critically implicated in the pathogenesis of a wide range of diseases, including autoimmune disorders,[10] age-related conditions,[11] cancer,[12] and various cardiovascular diseases.[13] Among these, their central role in the initiation and progression of AS is particularly well established.[14,15] Based on their *in vitro* activation states, macrophages are typically categorized into two main phenotypes – the classically activated M1 subtype and the alternatively activated M2 subtype.[16–18] M1 macrophages, upon activation, contribute to AS progression by producing a range of pro-inflammatory cytokines, such as IL-1β and TNF-α.[19,20] Conversely, M2 macrophages exert protective, anti-atherosclerotic functions by secreting anti-inflammatory mediators, including IL-10 and TGF-β, thereby promoting plaque regression and improving plaque stability.[21,22] Therefore, effectively modulating macrophage polarization from the pro-inflammatory M1 phenotype toward the anti-inflammatory M2 phenotype to improve the inflammatory microenvironment within AS plaques represents a theoretically promising therapeutic strategy.

Gold nanoparticles (AuNPs), one of the most extensively studied nanomaterials, can be engineered into various structures to modulate macrophage phenotypes.[23] They also possess favorable biological properties, including low cytotoxicity and minimal immunogenicity.[24,25] It has been reported that spherical AuNPs of an appropriate size exhibit anti-inflammatory effects and can induce the polarization of bone marrow-derived macrophages from the M1 phenotype to the M2 phenotype.[26] In addition, surface-modified AuNPs have shown great potential in biomedical imaging applications, including fluorescence imaging,[27] computed tomography imaging,[28] and photoacoustic (PA) imaging.[29] These features collectively position AuNPs as promising, safe, and effective theranostic tools for AS. However, the therapeutic efficacy of AuNPs alone remains limited due to suboptimal biodistribution and a lack of targeting specificity, which hampers their clinical utility and safety.[30] Therefore, developing strategies to achieve efficient and targeted delivery of AuNPs to lesion sites remains a major challenge and a key prerequisite for advancing this theranostic approach.

The intrinsic migratory capacity of immune cells toward inflamed sites, together with the development of bionic nanomaterials that exploit such biological targeting tendencies, has greatly advanced inflammation-targeted precision medicine.[31–34] Among these, macrophages are capable of sensing AS-associated cytokine signals and, owing to their innate biological targeting and inflammation-homing properties, can actively migrate to atherosclerotic lesions.[35–37] Leveraging this capability, live-cell engineering of macrophages enables the targeted delivery of therapeutic agents, potentially prolonging systemic circulation time while minimizing cytotoxicity to non-target cells and tissues.[38]

In this work, we designed an engineered macrophage-based probe (MφMB-Au) that carries AuNP-loaded ultrasound microbubbles (MB-Au) for the integrated diagnosis and therapy of AS. AuNPs play a dual role as both PA imaging agents and therapeutic modulators that promote M2 macrophage polarization. During AS progression, inflammatory cell infiltration and systemic cytokine release occur. Guided by these cytokine signals, intravenously administered MφMB-Au actively migrates toward inflamed atherosclerotic plaques (Fig. 1). Our results demonstrated that MφMB-Au retained its intrinsic inflammation-homing capability, allowing for the precise targeting of AS plaques. Moreover, this targeted delivery process can be dynamically monitored in real time using ultrasound (US)/photoacoustic (PA) imaging. *In vivo* studies have demonstrated that MφMB-Au exhibits superior therapeutic efficacy against AS.

2. Materials and methods

2.1 Antibodies and reagents

Antibodies against α-SMA and F4/80 were purchased from Cell Signaling Technology (Boston, USA). Antibodies against β-actin was purchased from Affinity Biosciences (California, USA). Antibodies against Arg-1 and CD206 were purchased from Proteintech Group (Wuhan, China). Brilliant violet 711™ anti-mouse CD4, brilliant violet 421™ anti-mouse CD25, PE anti-mouse Foxp3, APC anti-mouse CD3, brilliant violet 711™ anti-mouse CD4, brilliant violet 421™ anti-mouse IFN-γ, PE/cyanine7 anti-mouse IL-4 antibody, PE/cyanine7 anti-mouse F4/80 antibody, Alexa Fluor® 700 anti-mouse/human CD11b antibody, APC anti-mouse CD206 (MMR) antibody, PE anti-mouse CD86 antibody, APC/cyanine7 anti-mouse CD45 antibody, Zombie Yellow™ fixable viability kit and RBC lysis buffer were purchased from BioLegend (San Diego, CA, USA). Gold(III) chloride solution, sodium citrate tribasic dihydrate, HS-PEG-NH_2, anti-rabbit HRP-conjugated IgG secondary antibody, lipopolysaccharide (LPS), ammonium bicarbonate (NH_4HCO_3), and polyvinyl alcohol (PVA) were purchased from Sigma-Aldrich (St. Louis, MO, USA). Dulbecco's modified Eagle's medium (DMEM) and fetal bovine serum (FBS) were purchased from Invitrogen (CA, USA). 1,2-Distearoyl-*sn-glycero*-3-phosphocholine (DSPC) was obtained from Avanti Polar Lipids (AL, USA). Poly(DL-lactide-*co*-glycolide) (PLGA, 50 : 50, M_w = 30 000) was purchased from Jinan Daigang Biological Material (Shandong, China). Phalloidin-FITC Conjugate was obtained from Yeasen Biotechnology (Shanghai, China). 100× penicillin–streptomycin solution, 1,1′-dioctadecyl-3,3′,3′-tetramethylindocarbocyanine perchlorate (DiI) and 2-(4-amidinophenyl)-6-indolecarbamidine dihydrochloride (DAPI) were purchased from

This journal is © The Royal Society of Chemistry 2025

Open Access Article. Published on 23 December 2025. Downloaded on 1/24/2026 10:53:48 PM.
This article is licensed under a Creative Commons Attribution-NonCommercial 3.0 Unported Licence.

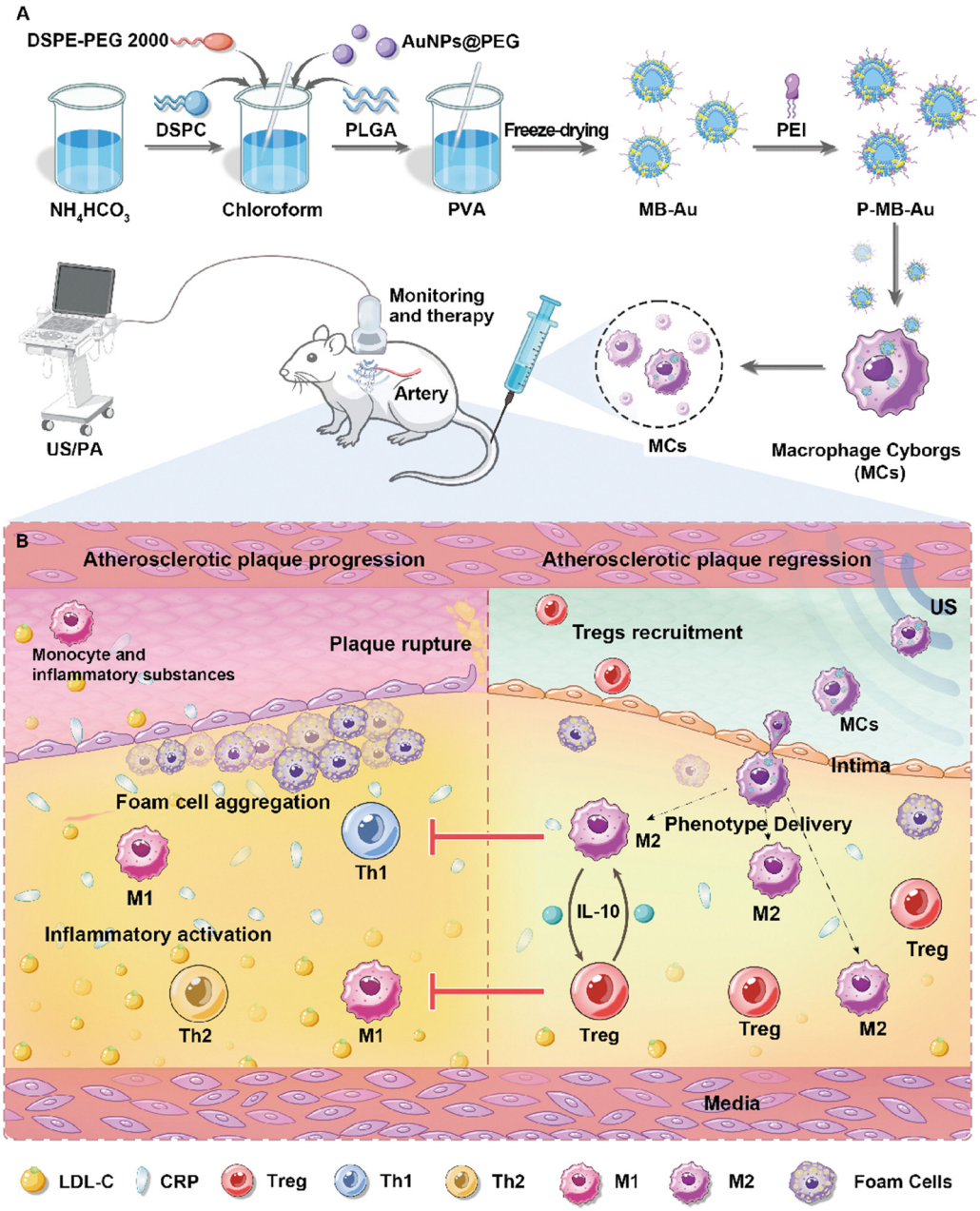

Fig. 1 Schematic diagram displaying the MφMB-Au fabrication, targeting, and its anti-AS properties.

Beyotime Biotechnology (Shanghai, China). Cell Counting Kit-8 was purchased from Servicebio (Wuhan, China).

2.2 Synthesis and characterization of AuNPs

As previously described,[39] polyethylene glycol (PEG)-functionalized gold nanoparticles (AuNPs) with diameters of 5, 25, 50, and 100 nm were synthesized through the reaction of citrate-stabilized gold nanoparticles with thiolated PEG. The morphology and size of AuNPs were characterized using transmission electron microscopy (TEM, JEOL, Japan). The hydrodynamic size distribution and zeta potential of the nanoparticles in aqueous solution were determined using a ZetaSizer Nano-ZS system (Malvern, UK). The optical extinction spectra of AuNPs were evaluated using UV-vis spectrophotometry (PerkinElmer Lambda, USA).

2.3 Synthesis and characterization of MB-Au

Based on our previously reported method,[40] 50 mg of PLGA and 2.5 mg of DSPC were dissolved in 1.0 mL of chloroform. To this organic phase, 0.2 mL of freshly prepared ammonium bicarbonate (NH_4HCO_3, 60 mg mL^{-1}) and 0.3 mL of PEGylated AuNPs were added. The mixture was emulsified using an ultrasonic probe in an ice bath for 2 minutes with a pulsed cycle (3 s on, 3 s off). The resulting emulsion was slowly added to 5 mL of 4% (w/v) polyvinyl alcohol (PVA) solution and homogenized at 6000 rpm for 5 minutes. Subsequently, 10 mL of pre-chilled

Open Access Article. Published on 23 December 2025. Downloaded on 1/24/2026 10:53:48 PM. This article is licensed under a Creative Commons Attribution-NonCommercial 3.0 Unported Licence.

deionized water was added, and the suspension was stirred at room temperature for 4 hours to allow organic solvent evaporation. The nanoparticles were collected by centrifugation at 6000 rpm and 4 °C for 10 minutes, washed three times with deionized water, and resuspended in 0.5 mL of deionized water. The final formulation was lyophilized for 24 hours to obtain MB-Au and stored at 4 °C. Using the same procedure, 2 μL of DiI fluorescent dye was incorporated into the organic phase to produce DiI-labeled MB-Au (DiI-MB-Au). MB-Au was further coated with polyethyleneimine (PEI) to confer a positive surface charge (P-MB-Au), thereby enhancing macrophage uptake and internalization. Scanning electron microscopy (SEM, Hitachi, Japan), energy-dispersive spectroscopy (EDS, AZtecLive, UK) and Fourier transform infrared spectroscopy (FTIR, Bruker-Optik, Germany) analyses were conducted to examine the structural features of MB-Au and to confirm the presence of AuNPs on its surface.

2.4 Cell culture

Mouse macrophage RAW264.7 cells (ATCC, TIB-71) were maintained in Dulbecco's modified Eagle's medium (DMEM) containing 10% fetal bovine serum (FBS) and 1% penicillin–streptomycin at 37 °C in a humidified incubator with 5% CO_2. Once cells reached approximately 80% confluence, they were gently harvested using a cell scraper and seeded into 6-well plates at a density of 3.0×10^5 cells per well for subsequent experiments.

To determine the optimal particle size and concentration of AuNPs for promoting M2 macrophage polarization, the following experiments were conducted: (i) size optimization: RAW264.7 macrophages were incubated with AuNPs of different diameters (25 nm, 50 nm, and 100 nm) at a fixed concentration of 0.1 mg mL^{-1} for 24 hours. After incubation, the AuNP-containing medium was removed, and cells were further cultured in complete medium for an additional 24 hours. The intracellular morphology of AuNPs was examined using TEM. The expression levels of M2 macrophage markers Arg-1 and CD206 were assessed at both the protein and mRNA levels using western blotting (WB) and quantitative PCR (qPCR) (Table S1), respectively. In addition, CD206 expression was evaluated by flow cytometry. (ii) Concentration optimization: RAW264.7 cells were treated with AuNPs at varying concentrations (0.2 mg mL^{-1}, 0.1 mg mL^{-1}, 0.05 mg mL^{-1}, and 0.01 mg mL^{-1}) for 24 hours, followed by co-incubation with lipopolysaccharide (LPS, 100 ng mL^{-1}) for 6 hours. The mRNA expression levels of Arg-1 and TNF-α were measured using qPCR to evaluate M2 and pro-inflammatory responses, respectively.

For omics analysis, RAW264.7 macrophages were divided into two groups: control cells were cultured under standard conditions without additional treatment, while experimental cells were incubated with 50 nm AuNPs at a concentration of 0.1 mg mL^{-1} for 24 hours, followed by an additional 24 hours of culture in the complete medium.

To validate the multi-omics findings, RAW264.7 cells were subjected to the following treatments: after adherence, the cells were switched to serum-free DMEM and serum-starved for 2 hours at 37 °C in a 5% CO_2 incubator. Subsequently, the cells were randomly divided into four groups: (1) control group: received an equivalent volume of the vehicle solvent DMSO; (2) fatostatin group: treated with 10 μM fatostatin; (3) AuNPs group: treated with 0.2 mg mL^{-1} AuNPs; (4) fatostatin + AuNPs combination group: pre-treated with 10 μM fatostatin for 4 hours, followed by co-treatment with 0.2 mg mL^{-1} AuNPs. All groups were then incubated under their respective treatment conditions for an additional 24 hours at 37 °C with 5% CO_2. Following treatment, the cells were harvested, and total RNA was extracted for qPCR analysis.

2.5 Cell viability assay

Cell viability was evaluated using the Alamar Blue assay (Solarbio, China), which provides a fluorescence read-out less affected by the optical properties of AuNPs. RAW264.7 cells were seeded in 96-well plates (0.5×10^4 cells per well) and treated with different concentrations of AuNPs (0.05, 0.1, 0.2, and 0.4 mg mL^{-1}) or MB-Au (0.5, 1.0, 2.0, and 4.0×10^8 mL^{-1}) for 24, 48, and 72 h. After incubation, 10 μL of Alamar Blue reagent was added to each well, followed by incubation at 37 °C for 2 h. Fluorescence intensity was measured at an excitation wavelength of 530 nm and an emission wavelength of 590 nm using a microplate reader (Spark, TECAN, Switzerland).

To eliminate background interference from the optical absorbance or scattering of AuNPs, wells containing the same concentrations of AuNPs or MB-Au in complete medium without cells were included as nanoparticle blanks (NP blanks). Their fluorescence values were subtracted from those of the corresponding sample wells. All experiments were performed in triplicate.

2.6 Construction and characterization of MφMB-Au

When RAW264.7 cells reached approximately 80% confluency, the culture medium was replaced with fresh medium containing P-MB-Au at a concentration of 2.0×10^8 mL^{-1}. After co-incubation for the indicated durations (1–8 h), the supernatant was removed and the cells were washed three times with PBS to eliminate unbound P-MB-Au, yielding MφMB-Au. To determine the optimal incubation time, MφMB-Au suspensions prepared at different time points (with equal MB-Au concentrations) were placed in phantom wells for contrast-enhanced ultrasound (CEUS) imaging, and the corresponding signal intensities were recorded (Fig. S4A). To evaluate the stability of MφMB-Au, MB-Au and MφMB-Au were dispersed in DMEM at equal concentrations and incubated at 37 °C; CEUS imaging was performed at different time points (1–4 h) and signal intensities were recorded. To compare the CEUS performance of MB-Au and MφMB-Au at equal concentrations, both were diluted to a series of concentrations and imaged under the same conditions, followed by quantitative analysis of signal intensity. TEM was employed to observe the intracellular morphology of MB-Au within RAW264.7 cells, while confocal laser scanning microscopy was used to assess the colocalization of red fluorescent DiI-labeled MB-Au with RAW264.7 cells.

This journal is © The Royal Society of Chemistry 2025

Open Access Article. Published on 23 December 2025. Downloaded on 1/24/2026 10:53:48 PM.
This article is licensed under a Creative Commons Attribution-NonCommercial 3.0 Unported Licence.

2.7 Transcriptomic and metabolomic analysis

Transcriptomic analysis was performed to investigate gene expression changes induced by AuNPs. Total RNA was extracted from RAW264.7 macrophages using a commercial RNA extraction kit, and RNA integrity was confirmed using an Agilent Bioanalyzer. RNA sequencing libraries were prepared and sequenced on the Illumina NovaSeq platform. Clean reads were aligned to the mouse reference genome using HISAT2, and differentially expressed genes (DEGs) were identified with DESeq2. Genes with $|\log_2$ fold change$| > 1$ and adjusted p-value < 0.05 were considered significantly different. The KEGG pathway enrichment analysis was performed to explore the biological functions of DEGs.

For metabolomics, cells were collected and metabolites were extracted using a methanol-based solvent system. Samples were analyzed by LC-MS/MS in both positive and negative ion modes. The raw data were processed with standard software, and metabolites were annotated using KEGG and HMDB databases. Differential metabolites were selected based on VIP > 1 and $p < 0.05$.

To investigate the relationship between gene expression and metabolic changes, an integrated analysis of transcriptomic and metabolomic data was conducted. Correlation heatmaps and nine-quadrant plots were used to identify key pathways and regulatory patterns associated with macrophage polarization.

2.8 Ultrasonic imaging *in vitro*

A total of 3 mg of agar powder was dissolved in 200 mL of ultrapure water, heated, and stirred continuously to form an agarose gel. The agarose solution was then poured into a mold to prepare hollow agarose phantoms for ultrasound imaging. MB-Au and Mφ-MB-Au were dispersed in ultrapure water to generate serial concentration gradients. These dispersions were injected into the hollow cavities of the agar blocks. Ultrasound imaging was performed using a VEVO 3100 (FUJIFILM VisualSonics, USA) system to visualize the samples within the side cavities of the agar phantoms. The relative positions of the phantom, dispersion, and probe are illustrated in Fig. 3C. Both B-mode and CEUS modes were employed for imaging. The ultrasound contrast intensity within the regions of interest was subsequently quantified using a dedicated imaging analysis system to assess concentration-dependent signal enhancement.

2.9 Photoacoustic imaging *in vivo*

Mice were anesthetized and placed in the supine position on a dedicated animal platform. Hair on the chest and upper abdomen was removed using a depilatory cream. The platform was then tilted 15° to the right, and the probe arm was tilted 45° to the left. The photoacoustic probe was lowered to the right side of the sternum, allowing clear visualization of the aortic arch and its major branches (Fig. S3). Subsequently, 200 μL of MB-Au or MφMB-Au (2.0×10^8 mL^{-1}) was intravenously injected *via* the tail vein. Real-time photoacoustic imaging was performed using the Vevo F2 LAZR-X20 system, and photoacoustic signals within the region of interest were recorded over time.

2.10 Evaluation of the targeting efficacy of MφMB-Au *in vivo*

ApoE$^{-/-}$ mice (4-week-old) were obtained from Vital River Laboratory Animal Technology (Beijing, China). All procedures involving animals were conducted in accordance with the guidelines approved by the Institutional Animal Care and Use Committee of Jinan University (Approval No. AUP-250515-LYY-0543-01). To promote the development of atherosclerosis, mice were maintained on a high-fat diet (HFD; 41% fat, 17% protein) for 8 weeks before subsequent treatments. Mice then received intravenous injections of saline, Mφ, MφMB, or MφMB-Au at a concentration of 2.0×10^8 mL^{-1}. Four hours post-injection, animals were euthanized, and systemic perfusion was performed using cold PBS supplemented with 4% paraformaldehyde. The isolated aortas were subjected to fluorescence imaging and quantification using the Xenogen IVIS 200 system.

2.11 Therapeutic performance of MφMB-Au *in vivo*

Following 8 weeks of HFD feeding, ApoE$^{-/-}$ mice were randomly divided into five groups (n = 4 per group): (1) saline control; (2) MB-Au; (3) Mφ; (4) MφMB; and (5) MφMB-Au. Each group received the corresponding treatment *via* a tail vein injection, and after 4 hours, ultrasound irradiation (1.5 W cm^{-2}, 30% duty cycle) was applied to the precordial region for 10 minutes. This treatment regimen was administered twice per week for a total of 8 weeks, during which all mice continued on the HFD.

At the end of the treatment period, body weight and photographs were recorded prior to euthanasia. Samples were collected as follows: (i) whole blood and spleen were harvested for flow cytometry analysis to quantify macrophage and T cell populations; (ii) the aortic arch was carefully dissected and imaged, and the heart along with the attached aorta was excised. The aorta was longitudinally sectioned for oil red O (ORO) staining to visualize atherosclerotic plaques. Serial 8-μm-thick cryosections of the heart were prepared for histological and immunohistochemical analysis, including hematoxylin and eosin (H&E), ORO, Masson's trichrome, and immunohistochemistry (IHC); (iii) major organs (heart, liver, spleen, lungs, and kidneys) were subjected to H&E staining to assess systemic biocompatibility and potential toxicity of the treatment.

2.12 *In vivo* biosafety evaluation of MφMB-Au

To evaluate the biosafety of MφMB-Au, 4-week-old ApoE$^{-/-}$ mice were randomly divided into two groups (n = 3 per group): (1) saline control group: injected intravenously with 200 μL saline; (2) MφMB-Au experimental group: injected intravenously with 200 μL MφMB-Au. Administrations were performed weekly *via* tail vein injection for a total of four injections over four weeks. All mice were fed a high-fat diet throughout the study period. Seven days after the final injection, whole blood was collected *via* retro-orbital bleeding under anesthesia. Blood samples were centrifuged (4 °C, at 3000 rpm for 20 min) to obtain serum. The collected serum was then analyzed for the

Open Access Article. Published on 23 December 2025. Downloaded on 1/24/2026 10:53:48 PM. This article is licensed under a Creative Commons Attribution-NonCommercial 3.0 Unported Licence.

following parameters: (1) liver function, cardiac metabolite, and serum lipid profiles: serum levels of alanine aminotransferase (ALT), aspartate aminotransferase (AST), blood urea nitrogen (BUN), creatine kinase MB isoenzyme (CK-MB), triglycerides (TG), total cholesterol (CHO), and high-density lipoprotein cholesterol (HDL) were measured; (2) inflammatory cytokine analysis: serum levels of tumor necrosis factor-alpha (TNF-α), interleukin-6 (IL-6), and interferon-gamma (IFN-γ) were quantified; (3) anti-PEG antibody titer determination: the serum titer of anti-polyethylene glycol (PEG) antibodies was assessed.

2.13 Statistical analysis

Statistical analyses were performed using SPSS software (version 17.0; SPSS Inc., USA). Data are presented as mean ± standard error of the mean (SEM). Comparisons between two groups were analyzed using two-tailed unpaired Student's *t*-tests. For comparisons among three or more groups, one-way ANOVA was performed, followed by Tukey's honestly significant difference *post hoc* test. Statistical significance was thresholded at $p < 0.05$.

3. Results and discussion

3.1 Characterization of AuNPs, MB-Au and MφMB-Au

Polyethylene glycol (PEG)-functionalized AuNPs with diameters of 5, 25, 50, and 100 nm were fabricated using a chemical reduction approach. The nanoparticles were analyzed using transmission electron microscopy (TEM), dynamic light scattering (DLS), and ultraviolet-visible (UV-vis) spectroscopy. The TEM examination indicated that the resulting AuNPs were nearly spherical and demonstrated highly monodispersity (Fig. 2A). Both DLS and TEM analyses confirmed the particle sizes, with average diameters of 5, 25, 50, and 100 nm, for the respective samples (Fig. 2B and C). The UV-vis extinction spectra exhibited size-dependent shifts in the localized surface plasmon resonance peaks, with maxima observed at 520, 529, 543, and 578 nm for the 5, 25, 50, and 100 nm AuNPs,

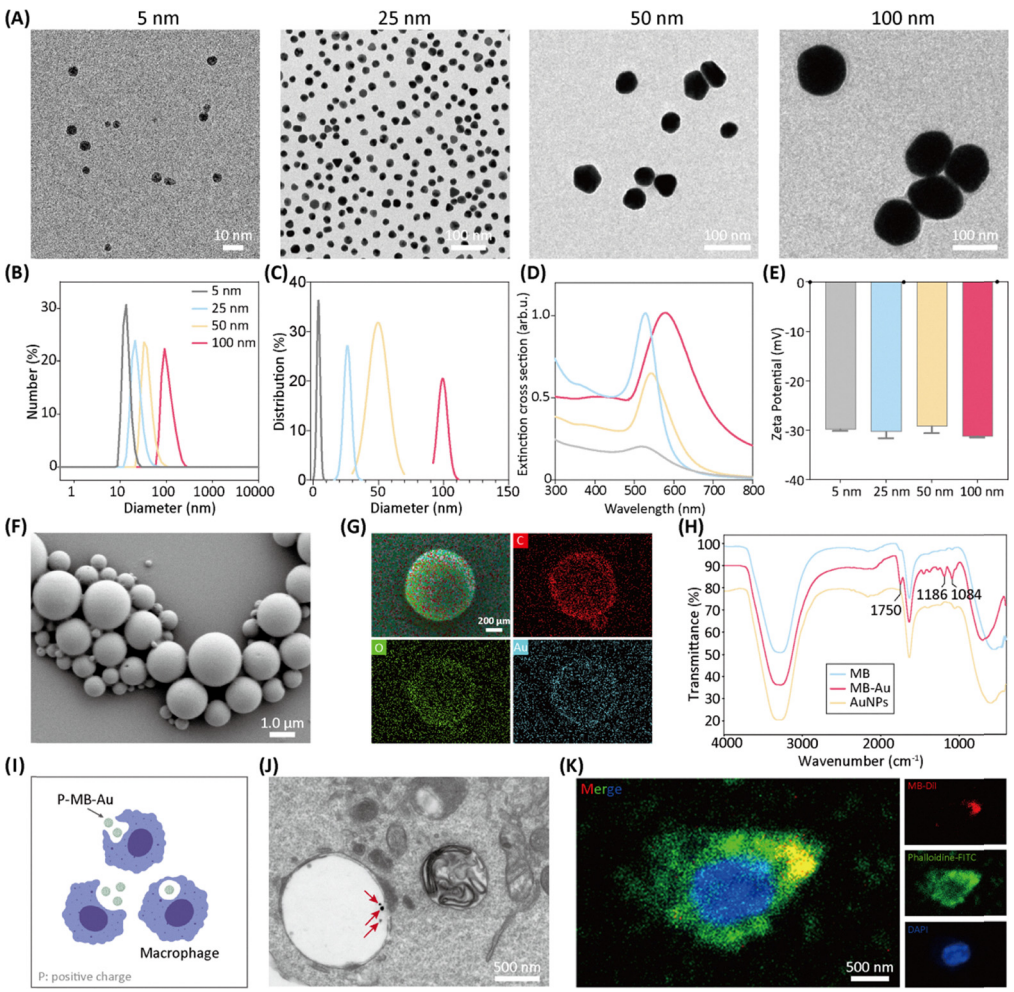

Fig. 2 Characterization of AuNPs, MB-Au and MφMB-Au (A) TEM images of AuNPs at different sizes. Size distribution of AuNPs analyzed by DLS (B) and TEM (C), respectively. UV-Vis extinction spectra (D) and zeta potential (E) of AuNPs with different sizes. SEM (F) and EDS (G) images of MB-Au. (H) FTIR spectral analysis of MB, MB-Au and AuNPs. (I) Schematic diagram illustrating the construction of MφMB-Au. (J) TEM images of the MφMB-Au, while (K) displays confocal microscopy images of the probes. Red arrows indicate AuNPs.

 This journal is © The Royal Society of Chemistry 2025

Open Access Article. Published on 23 December 2025. Downloaded on 1/24/2026 10:53:48 PM. This article is licensed under a Creative Commons Attribution-NonCommercial 3.0 Unported Licence.

respectively (Fig. 2D). The zeta potential measurements yielded values of -29.8 ± 0.54 mV, -30.3 ± 2.65 mV, -29.2 ± 3.12 mV, and -31.2 ± 0.72 mV for the 5 nm, 25 nm, 50 nm, and 100 nm AuNPs, respectively, confirming that all samples exhibited negatively charged surfaces.

It has been reported that AuNPs can directly induce M2 macrophage polarization.[41] To evaluate the immunomodulatory effects of AuNPs on macrophages, we first compared particles of different diameters. As shown in Fig. S1A, AuNPs of 25, 50, and 100 nm were efficiently internalized by macrophages. Consistent with previous studies,[42–44] 5 nm AuNPs were not included in subsequent experiments because they are known to exhibit markedly higher cytotoxicity across multiple cell types at equivalent mass concentrations, and our data similarly showed that 5 nm particles did not induce significant changes in either M1- or M2-associated gene expression compared with the control group (Fig. S1B). Analysis of macrophages treated with 25, 50, or 100 nm AuNPs revealed that 50 nm particles elicited the most robust enhancement of M2 polarization, as demonstrated by increased Arg-1 and CD206 expression at both the mRNA and protein levels (Fig. S1B–F). Further concentration-gradient experiments confirmed an optimal effective dose of 0.2 mg mL^{-1} for 50 nm AuNPs (Fig. S1G and H). Therefore, AuNPs with a diameter of 50 nm at 0.2 mg mL^{-1} were selected for all subsequent mechanistic studies.

Using the same preparation method,[40] we successfully synthesized AuNP-loaded microbubbles (MB-Au). Scanning electron microscopy (SEM) images demonstrated that MB-Au possesses a hollow spherical morphology (Fig. 2F). Complementary energy-dispersive X-ray spectroscopy (EDS) confirmed the presence of carbon (C), oxygen (O), and gold (Au) in the MB carrier, verifying the successful loading of AuNPs onto the MB (Fig. 2G). Fourier transform infrared (FTIR) spectroscopy further confirmed the presence of AuNPs on MB-Au.

Cell-based therapies have been clinically applied to treat a wide range of diseases.[45–47] Here, we developed an engineered macrophage probe (MφMB-Au) on living cells. Specifically, as illustrated in Fig. 2I, positively charged MB-Au nanoparticles were co-incubated with macrophages to construct the MφMB-Au platform. Fig. 2J shows TEM images of MB-Au internalized by macrophages, revealing the presence of punctate AuNPs. Additionally, MB-Au was labeled with DiI, and confocal microscopy confirmed the co-localization of MB-Au with macrophages, demonstrating the successful uptake of MB-Au by the MφMB-Au (Fig. 2K).

To this end, we successfully synthesized a series of AuNPs using a chemical reduction method. The optimal diameter and concentration of AuNPs for promoting M2 polarization were identified through WB, qPCR, and FC analyses. Additionally, AuNP-loaded microbubbles were successfully prepared *via* a double emulsion evaporation method and subsequently co-incubated with macrophages, resulting in the successful development of MφMB-Au.

3.2 Omics analysis and pathway validation of AuNP-treated macrophages

Advances in transcriptomic and metabolomic profiling have significantly enhanced insights into complex biological processes and biomarker discovery.[48] As demonstrated above, AuNPs are capable of directly inducing M2 macrophage polarization. To further elucidate the underlying mechanisms, we performed integrated transcriptomic and metabolomic analyses.

To investigate the metabolic alterations induced by AuNPs, ultra-performance liquid chromatography-tandem mass spectrometry was employed to profile the metabolomic features of AuNP-treated macrophages. A total of 1121 metabolites were identified across both groups (Fig. S2A), with the majority classified as organic acids and their derivatives (16.32%). Principal component analysis (PCA) revealed a clear separation between the control and treatment groups (Fig. S2B), indicating distinct metabolic profiles. Following filtering criteria (fold change <0.5 or >2.0 and p-value <0.05), 113 differentially expressed metabolites were identified, including 90 upregulated and 23 downregulated metabolites in the treatment group compared to the control. This is visualized in the volcano plot (Fig. S2C). The KEGG enrichment analysis of the metabolomics data indicated a prominent involvement of pathways related to lipid and energy metabolism, such as fatty acid metabolism, AMPK signaling, and cholesterol metabolism. These pathways are known to play crucial roles in regulating macrophage M2 polarization and anti-inflammatory responses.[49,50] We further analyzed the enriched pathways of these differential metabolites using MetaboAnalyst (Fig. S2E). The results highlighted glycerophospholipid metabolism as one of the top altered pathways in differential metabolites. This is consistent with lipidomic studies showing an increased incorporation of exogenous fatty acids into glycerophospholipids in M2 macrophages, thereby supporting their anti-inflammatory phenotype.[51] Additionally, glutathione metabolism emerged as significantly enriched, echoing recent findings that glutathione-related genes are linked to M2 macrophage polarization in tumor microenvironments.[52]

In addition, we performed RNA-seq transcriptomic analysis to investigate gene expression profiles and functional annotations. Violin plot visualization demonstrated global gene expression density and variability, indicating consistent transcriptomic profiles among biological replicates (Fig. S3A). The PCA plot revealed strong consistency among the biological replicates within each group in addition to distinct transcriptomic differences between the groups (Fig. 3A). A heat map of differentially expressed genes revealed distinct expression patterns between the control and treatment groups (Fig. S3B). Compared with the control group, 188 genes were upregulated and 79 downregulated in the treatment group (Fig. 3B). Transcriptomic KEGG analysis indicated that fatty acid degradation, fatty acid metabolism, and TGF-β signaling were significantly enriched, all of which are implicated in M2 macrophage polarization (Fig. S3C). The GSEA results suggested that AuNPs may exert anti-inflammatory effects by reducing IL-1 production and enhancing cholesterol metabolism (Fig. 3C and D). A reactome-based chord diagram revealed the enrichment of pathways (Fig. S3D). We further analyzed the expression of key genes following AuNP treatment. The results showed

Open Access Article. Published on 23 December 2025. Downloaded on 1/24/2026 10:53:48 PM.
This article is licensed under a Creative Commons Attribution-NonCommercial 3.0 Unported Licence.

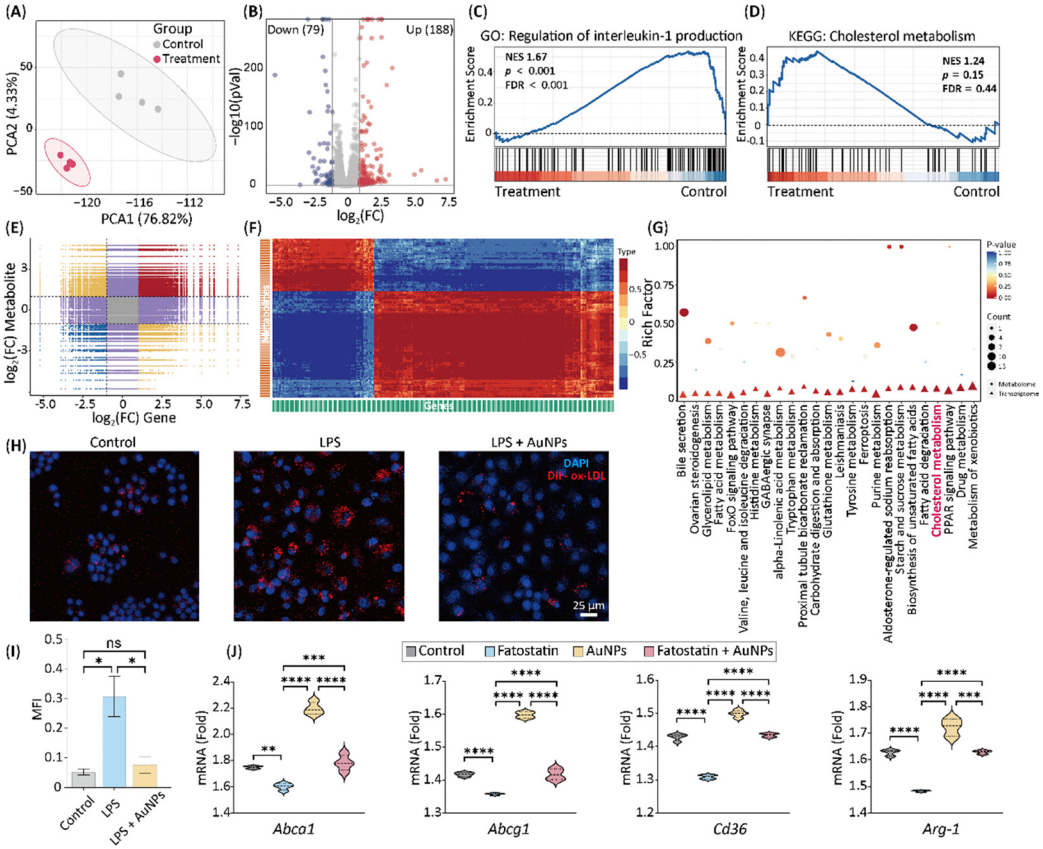

Fig. 3 Omics and pathway validation in AuNP-treated macrophages (A) PCA plot of RNA-seq data. (B) Volcano plot showing significantly upregulated (red) and downregulated (blue) genes. (C) and (D) GSEA of the "regulation of IL-1" and "cholesterol metabolism". NES, normalized enrichment score; FDR, false discovery rate. (E) and (F) Nine-quadrant plot and correlation heatmap integrating transcriptomic and metabolomic data, respectively. (G) Bubble plots of KEGG pathway enrichment analysis based on transcriptomic and metabolomic data. (H) IF images illustrating AuNP-enhanced cholesterol metabolism. (I) Quantification of fluorescence intensity corresponding to panel H. (J) qPCR analysis of ABCA1, ABCG1, CD36, and Arg1 expression.

significant up-regulation of MMP12 (a matrix metalloproteinase involved in tissue remodeling and repair), CXCL3 (a chemokine involved in promoting T cell recruitment), and ABCA1 (a cholesterol efflux transporter regulating lipid metabolism). In contrast, the pro-inflammatory gene TNFSF14 was markedly downregulated after AuNP exposure (Fig. S3E).

Finally, we integrated transcriptomic and metabolomic data using a nine-quadrant diagram combined with a correlation-based clustering heatmap (Fig. 3E and F) to explore the relationship between gene expression changes and metabolite alterations. Genes and metabolites were classified according to their up-regulation, down-regulation, or unchanged status, facilitating the identification of concordant or discordant regulatory patterns and uncovering key pathways involved in AuNP-induced macrophage polarization. The results revealed that AuNPs primarily modulate macrophage polarization through pathways related to cholesterol metabolism, as demonstrated by the integrated transcriptomic and metabolomic analyses (Fig. 3G).

To validate these multi-omics findings, we further performed immunofluorescence (IF) staining, combined with the strong M2-promoting effect of AuNPs observed in Fig. S1C. Consistently, AuNP treatment reduced intracellular lipid accumulation and enhanced lipid metabolic activity in macrophages (Fig. 3H and I). Mechanistically, AuNPs simultaneously increased the expression of the lipid-uptake receptor CD36 and the cholesterol-efflux transporters ABCA1 and ABCG1. Notably, the upregulation of ABCA1 (approximately 1.26-fold *vs.* control) exceeded that of CD36 (approximately 1.05-fold), resulting in a net reduction of intracellular lipid deposition, decreased foam-cell formation, and promotion of M2 polarization. This regulatory effect was abolished by fatostatin, a known inhibitor of the SREBP1/2 pathway, which consequently suppresses multiple downstream mechanisms involved in cholesterol efflux.[53]

3.3 Visualization research of MφMB-Au *in vitro*/*in vivo*

Engineered macrophages can serve not only as a drug delivery vehicle but also as a tool for targeted tracing.[36,37] The results demonstrated that both AuNPs and MB-Au exhibited a dose-dependent cytotoxicity profile, showing relatively higher cell viability at low concentrations but gradually reduced viability with increasing nanoparticle concentration and incubation time, consistent with previous studies,[54] which was particularly evident for AuNPs at 72 h (Fig. 4A). Based on these viability data, the working concentrations that maintained acceptable

This journal is © The Royal Society of Chemistry 2025

Open Access Article. Published on 23 December 2025. Downloaded on 1/24/2026 10:53:48 PM.
This article is licensed under a Creative Commons Attribution-NonCommercial 3.0 Unported Licence.

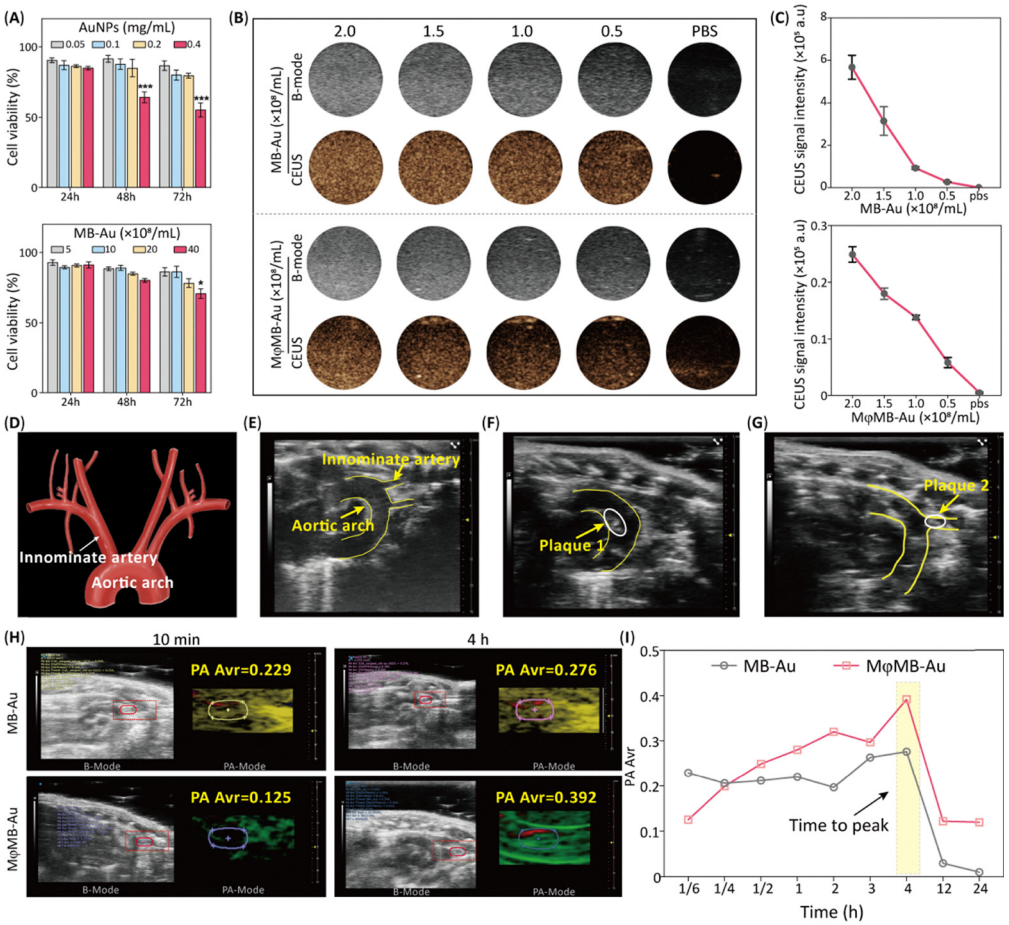

Fig. 4 Tracing study of MφMB-Au *in vitro* and *in vivo* (A) assessment of cytotoxicity of AuNPs and MB-Au on macrophages using the Alamar Blue assay. Data are presented as mean ± SD (n = 3). *$p < 0.05$, ***$p < 0.001$ *vs.* all other groups. (B) Contrast-enhanced ultrasound images of MB-Au and MφMB-Au at varying concentrations, with (C) corresponding quantitative statistical analysis. (D) Anatomical diagram of the aortic arch. (E) Two-dimensional ultrasound image of the aortic arch in healthy mice. (F) Hyperechoic plaques observed in the aortic arch of AS model mice. (G) Hyperechoic plaques detected at the pulseless artery in AS model mice. (H) and (I) Temporal variation of photoacoustic signals from MB-Au and MφMB-Au at different time points, measured at the pulseless artery plaques.

cytocompatibility were selected for subsequent imaging studies. Representative TEM and CEUS analyses further clarified that the ultrasound contrast signals originated from MB or MB-Au rather than AuNPs after co-incubation with macrophages (Fig. S4F). Subsequently, CEUS was employed to determine the optimal construction time of MφMB-Au (Fig. S4A). The results demonstrated that a 4-hour co-incubation of MB-Au with macrophages generated the highest yield of MφMB-Au particles, with CEUS signal intensities remaining essentially unchanged between 4 and 6 hours (Fig. S4B and D). We further evaluated the stability of both MB-Au and MφMB-Au (Fig. S4C and E). Owing to the inherent viability of macrophages, MφMB-Au maintained a prolonged imaging duration of up to 4 hours, whereas MB-Au exhibited a rapid loss of ultrasound signal, becoming nearly undetectable after 2 hours in DMEM at 37 °C. These findings suggest that intracellularly protected MBs exhibit enhanced stability and enable prolonged imaging performance. In addition, we evaluated the concentration-gradient imaging capabilities of MB-Au and MφMB-Au. The results demonstrated that both agents enabled concentration-dependent ultrasound imaging (Fig. 4B), with MB-Au exhibiting an approximately 30-fold higher signal intensity compared to MφMB-Au (Fig. 4C). These findings underscore the superior imaging persistence of living cell-based carriers, confirming the feasibility of using MφMB-Au for stable ultrasound imaging *in vitro*.

Subsequently, we assessed the PA imaging performance of MB-Au and MφMB-Au using a similar approach. Both agents exhibited a peak photoacoustic signal at 690 nm (Fig. S5A). At this wavelength, MB-Au and MφMB-Au demonstrated clear concentration-dependent photoacoustic signals, which are critical for enabling effective *in vivo* imaging applications (Fig. S5A and B). Following this, we employed ApoE$^{-/-}$ mice that were fed a high-fat diet for 8 weeks to validate *in vivo* PA imaging. Fig. 4D illustrates the anatomical diagram of the mouse aortic arch, highlighting the innominate artery, the brachiocephalic artery, the left common carotid artery, and the left subclavian artery, which are predisposed to AS due to hemodynamic factors.[36,37,55] Fig. 4E presents an ultrasound two-dimensional

Open Access Article. Published on 23 December 2025. Downloaded on 1/24/2026 10:53:48 PM. This article is licensed under a Creative Commons Attribution-NonCommercial 3.0 Unported Licence.

image of the aortic arch in healthy mice, showing a smooth intima with no apparent abnormal echoes. In contrast, the AS mice exhibited high-echogenic plaque shadows in the aortic arch and brachiocephalic artery (Fig. 4F and G). Given the significant mobility of the aortic arch, which is suboptimal for photoacoustic imaging, the innominate artery was selected as the region of interest for photoacoustic imaging in this study. As shown in Fig. 4H and I, we investigated the temporal changes in photoacoustic signals from plaques within the innominate artery for MB-Au and MφMB-Au at various time points. The results revealed that the photoacoustic signal intensity within the plaques peaked at 4 hours post-injection. Subsequently, the signal gradually declined, with the MB-Au group exhibiting near-zero signal intensity by 24 hours, whereas the MφMB-Au group maintained a relatively strong photoacoustic signal. MφMB-Au enables both US and PA imaging *in vitro*/*vivo*. Furthermore, our engineering modifications to macrophages did not alter their inherent inflammatory chemotactic properties (Fig. S6).

3.4 Therapeutic efficacy against AS

Building on these encouraging findings, we evaluated the therapeutic efficacy of MφMB-Au in an AS mouse model. As outlined in the treatment protocol depicted in Fig. 5A, four-week-old ApoE$^{-/-}$ mice were fed a high-fat diet for eight weeks to induce atherosclerotic pathology. Following this, an eight-week treatment regimen was administered, during which the various treatment modalities had no significant impact on the body weight of the mice ($p > 0.05$, Fig. 5B). After the treatment period, the mice were euthanized, and the aortic arch was meticulously dissected. As shown in Fig. 5C, white plaques were macroscopically visible on the vessel wall. Subsequently, the entire aorta was isolated and subjected to oil red O (ORO) staining for the quantitative assessment of plaque burden. As illustrated in Fig. 5C, the saline-treated group exhibited the highest plaque burden, with lesions occupying 37.48% of the total aortic area. In contrast, treatment with MB-Au, Mφ, and MφMB resulted in moderate reductions in the plaque area, achieving 25.80%, 28.57%, and 28.62%, respectively. Notably, the MφMB-Au-treated group demonstrated a significant reduction in the lesion area, which decreased to 17.06% of the total aortic area. These results suggest that MφMB-Au exhibits favorable biosafety while demonstrating potent anti-AS effects.

Following this, frozen sections of the aortic root were subjected to comprehensive histological analysis, including hematoxylin and eosin (HE) staining, oil red O (ORO) staining, Masson's trichrome staining, and immunohistochemistry (IHC). As depicted in Fig. 4D and E, HE staining of the aortic root in the saline-treated group revealed extensive plaque formation and prominent necrotic cores. In contrast, the MB-Au-, Mφ-, and MφMB-treated groups exhibited significant reductions in AS plaque formation, with plaque area reductions of approximately 33.45%, 38.55%, and 37.89% ($p < 0.05$), respectively. Notably, the MφMB-Au-treated group demonstrated the most substantial therapeutic effect, achieving a 41.38% reduction in the AS plaque area ($p < 0.001$).

ORO staining further revealed a marked reduction in lipid accumulation within AS plaques in the therapeutic groups (MB-Au, Mφ, MφMB, and MφMB-Au) compared to the saline control group (Fig. 5D and F). A quantitative analysis indicated that lipid deposition constituted 9.87% of the total plaque area in the saline-treated group. Potentially due to the anti-inflammatory properties of AuNPs, the MB-Au treatment group exhibited a modest reduction in lipid deposition (approximately 8.13%, $p > 0.05$) compared to the saline group. Conversely, the Mφ and MφMB treatment groups showed slight increases in lipid deposition (approximately 11.19% and 12.92%, respectively; $p > 0.05$) compared to the saline group, which can be attributed to the introduction of exogenous macrophages. In contrast, the MφMB-Au treatment group, leveraging the inflammation-targeting capability of macrophages carrying MB-Au, demonstrated enhanced accumulation in the AS plaque regions. This facilitated the ultrasound-mediated release of AuNPs, promoting M2 polarization and eliciting anti-inflammatory and anti-lipid deposition effects. This resulted in a significant reduction in lipid deposition (approximately 33.54%) compared to the saline group.

Masson's trichrome staining (Fig. 5D and G) revealed collagen deposition across the experimental groups. The saline group (8.93%), MB-Au group (7.11%), Mφ group (7.53%), and MφMB group (5.83%) exhibited no significant differences in the collagen content. In contrast, the MφMB-Au group displayed the highest collagen and α-SMA content (approximately 13.09% and 3.04%, respectively; Fig. 5J), which are critical for maintaining plaque stability.

Macrophages are involved in the entire pathological process of AS, playing a central role in progression.[38] In this study, we investigated whether MφMB-Au modulates macrophage infiltration within AS plaques. IHC analysis of the macrophage marker F4/80 (Fig. 5H and I) revealed a significant reduction in macrophage infiltration into plaques in the MφMB-Au treatment group, corresponding to approximately 11.62% of that observed in the saline control group ($p < 0.005$). Using the formula provided in Fig. S7, we quantified the impact of MφMB-Au on plaque vulnerability. Given the effects of MφMB-Au on lipid accumulation, macrophage infiltration, and collagen content, MφMB-Au treatment was associated with enhanced AS plaque stability compared to saline, as evidenced by an approximately 64.55% reduction in the plaque vulnerability index (PVI, Fig. 5K). Elevated PVI is correlated with a higher risk of adverse cardiovascular events.[1] Consequently, the intravenous administration of MφMB-Au may represent an additional therapeutic strategy to mitigate the risk of secondary events in patients with cardiovascular disease.

Our findings demonstrate that MφMB-Au effectively attenuates AS progression by reducing lipid deposition, suppressing macrophage infiltration, ameliorating the inflammatory microenvironment within plaques, and enhancing AS plaque stability.

3.5 Immune-modulatory properties of MφMB-Au

Both innate and adaptive immune responses are actively involved and become progressively activated throughout the

 This journal is © The Royal Society of Chemistry 2025

Open Access Article. Published on 23 December 2025. Downloaded on 1/24/2026 10:53:48 PM.
This article is licensed under a Creative Commons Attribution-NonCommercial 3.0 Unported Licence.

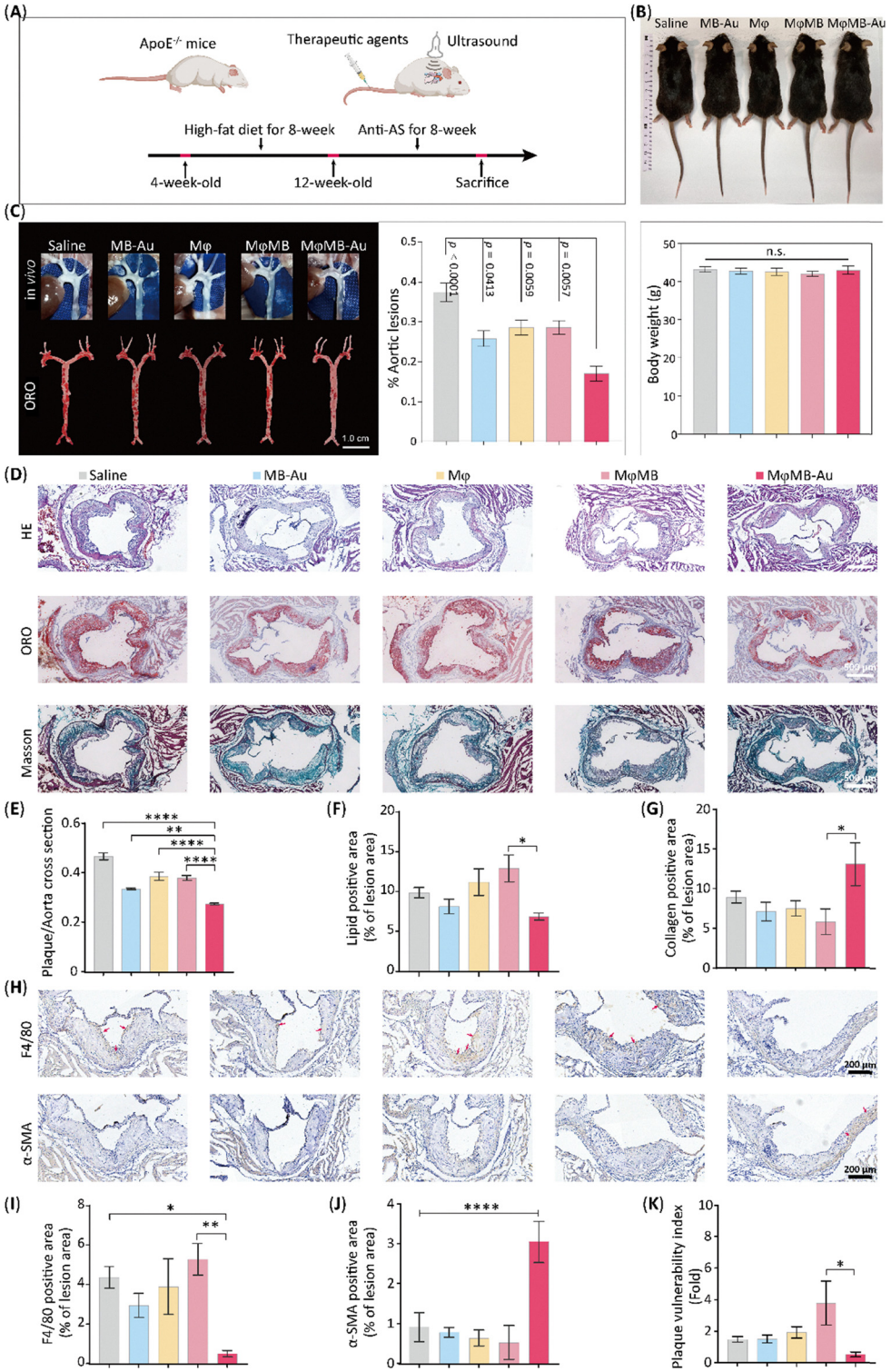

Fig. 5 The anti-AS effect of MφMB-Au (A) schematic representation of the treatment protocol in this study. (B) Post-treatment photographs of mice and statistical analysis of body weight. (C) *Ex vivo* imaging of the aortic arch (upper panel), gross oil red O staining of the aorta (lower panel), and quantitative analysis of lipid deposition. (D) Histological staining of aortic root sections with HE, ORO, and Masson's trichrome. (E) Quantitative analysis of the plaque area in HE-stained sections. (F) Quantitative analysis of lipid deposition in ORO-stained sections. (G) Quantitative analysis of collagen deposition in Masson's trichrome-stained sections. (H) IHC staining of aortic root sections for F4/80 and α-SMA. (I) Quantitative analysis of F4/80-positive area. (J) Quantitative analysis of α-SMA-positive area. (K) Plaque vulnerability index (PVI) of mice subject to different treatments.

Open Access Article. Published on 23 December 2025. Downloaded on 1/24/2026 10:53:48 PM.
This article is licensed under a Creative Commons Attribution-NonCommercial 3.0 Unported Licence.

development and progression of AS.[56] Regulatory T cells (Tregs) have been shown to be atheroprotective, whereas Th1 cells exert pro-atherogenic effects by sustaining and amplifying inflammatory responses through the secretion of IFN-γ.[57–59] Therefore, we subsequently evaluated the changes in the content and proportion of macrophages (M0, M1 and M2) and T-cell subsets (Th1, Th2, and Treg) in the spleen and peripheral blood of mice before and after treatment (Fig. 6A).

Flow cytometry data were analyzed using a standardized gating strategy with fluorescence minus one (FMO) control to ensure accurate identification of positive populations (Fig. S8). In the spleen (Fig. 6B–J), there were no significant differences among the groups in the total number of macrophages or M1 macrophages; however, the MφMB-Au group exhibited a marked increase in M2 macrophage levels, approximately 5.3-fold higher than those in the saline group. Correspondingly,

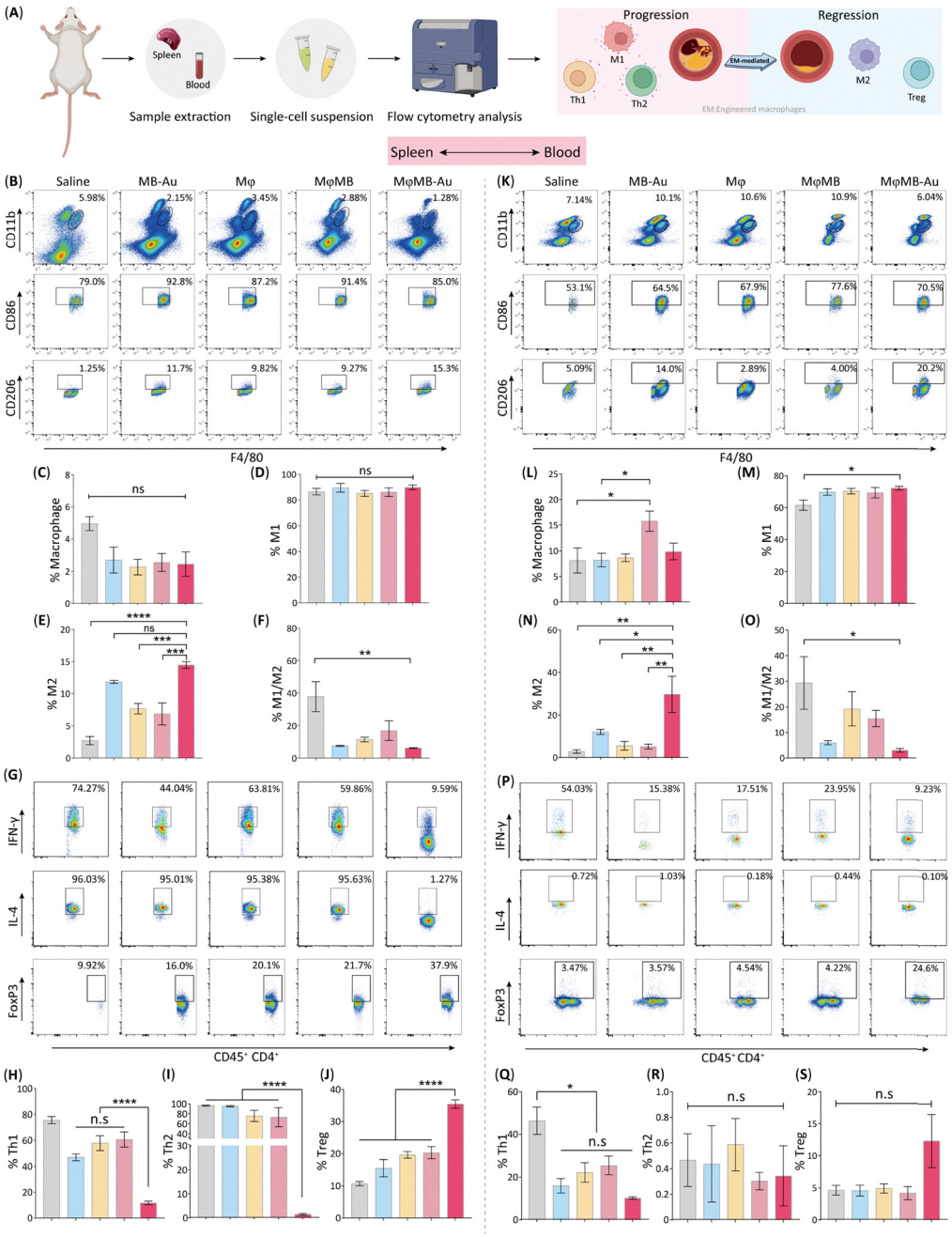

Fig. 6 Immunomodulatory effects of MφMB-Au (A) schematic illustration of mouse spleen and peripheral blood sample processing, flow cytometry analysis, and intercellular regulatory interactions. (B)–(F) Flow cytometry quantification of total macrophages, M1 and M2 macrophage populations, and the M1/M2 ratio in the spleens of each group. (G)–(J) Flow cytometry analysis of Th1, Th2, and Treg cell populations in mouse spleens across different treatment groups. (K)–(O) Flow cytometry quantification of total macrophages, M1 and M2 macrophages, and the M1/M2 ratio in peripheral blood samples. (P)–(S) Flow cytometry analysis of Th1, Th2, and Treg cell populations in the peripheral blood of each group.

This journal is © The Royal Society of Chemistry 2025

Open Access Article. Published on 23 December 2025. Downloaded on 1/24/2026 10:53:48 PM.
This article is licensed under a Creative Commons Attribution-NonCommercial 3.0 Unported Licence.

the M1/M2 ratio was significantly reduced by 83.53% in the MφMB-Au group. Additionally, this group showed a notable decrease in Th1 and Th2 cell proportions, while Treg cell levels were significantly elevated, reaching 3.3 times those of the saline group. In peripheral blood (Fig. 6K–S), total macrophage levels were slightly increased in the MφMB-Au group, and the trends in M1, M2, and M1/M2 macrophages mirrored the results observed in the spleen. While the Th1 cell levels were reduced in all treatment groups compared to the saline group, the differences were not statistically significant. The Th2 cell levels remained comparable across all groups. Notably, although the increase in Treg cells in the MφMB-Au group did not reach statistical significance compared to the other groups, their levels were approximately 2.7-fold higher than those in the saline group. These findings indicate that the MφMB-Au treatment alleviates systemic inflammation by modulating macrophage polarization (reduced M1/M2 ratio) and enhancing Treg-mediated suppression of pro-inflammatory Th1/Th2 responses, contributing to its anti-AS efficacy. Collectively, the combined use of ultrasound/photoacoustic imaging and the mechanistic identification of the ABCA1 axis driving M2 polarization, make the novel MφMB-Au platform promising candidates for AS theragnostics strategy (Table S2).

3.6 Biocompatibility of MφMB-Au

After an 8-week treatment period, we evaluated the potential side effects associated with various therapeutic strategies. Our findings showed that none of the treatment groups exhibited significant changes in body weight (Fig. 5B). In addition, H&E staining revealed no evident histopathological alterations in major organs, including the heart, liver, spleen, lungs, or kidneys (Fig. S9). To further evaluate systemic biosafety and immunogenicity, ApoE$^{-/-}$ mice received repeated intravenous administrations of MφMB-Au once per week for three weeks (Fig. 7E). Serum biochemistry analysis demonstrated that ALT, AST, BUN, and CK-MB levels remained comparable to those of the saline-treated group, indicating the absence of hepatic, renal, or cardiac toxicity (Fig. 7A and B). Inflammatory cytokines (IL-6 and TNF-α) also showed no significant elevation, and IFN-γ levels were below the detection threshold, suggesting no cytokine-storm-related immune activation (Fig. 7C).

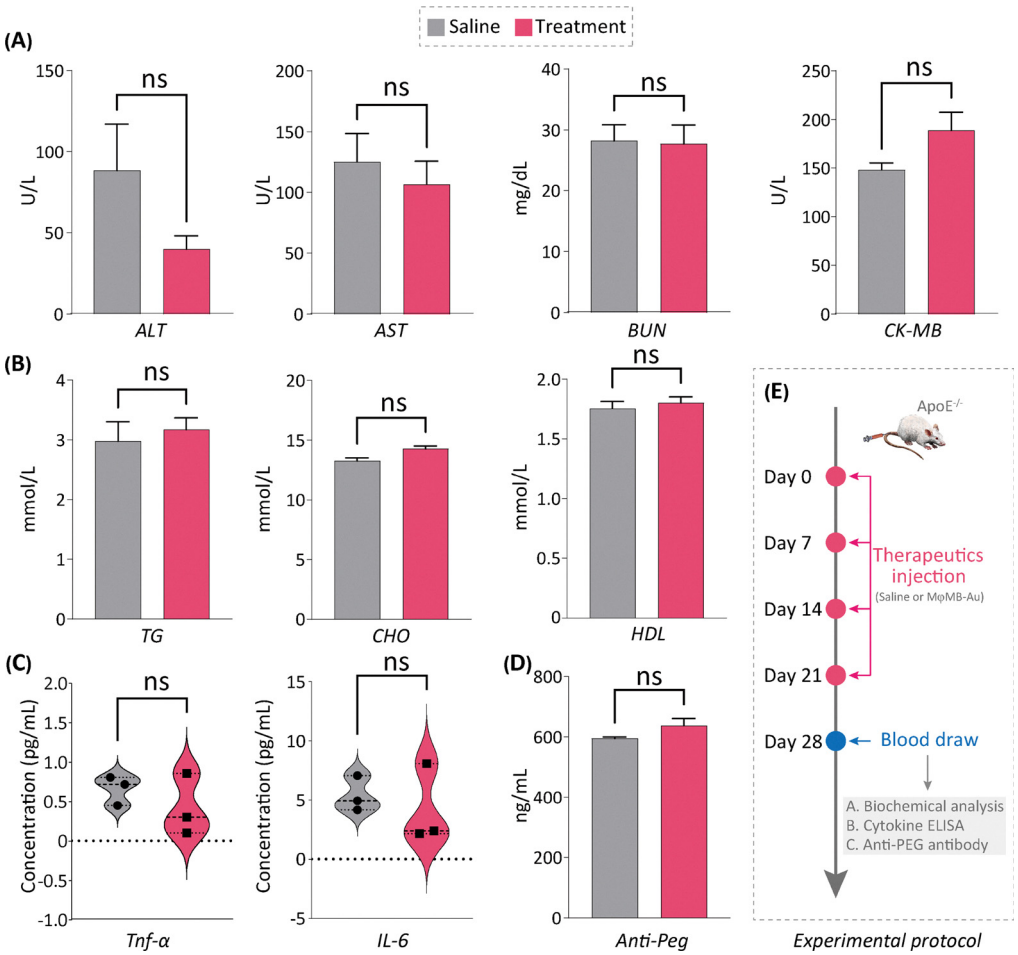

Fig. 7 Evaluation of the biocompatibility of MφMB-Au (A) serum biochemical markers including ALT, AST, BUN, and CK-MB. (B) Lipid profiles in serum. (C) Serum levels of inflammatory cytokines TNF-α and IL-6. (D) Serum anti-PEG antibody titers. (E) Schematic of the animal treatment protocol.

Open Access Article. Published on 23 December 2025. Downloaded on 1/24/2026 10:53:48 PM. This article is licensed under a Creative Commons Attribution-NonCommercial 3.0 Unported Licence.

Moreover, the anti-PEG antibody titers exhibited no significant differences between the two groups following repeated dosing, confirming minimal immunogenicity of the PEGylated formulation (Fig. 7D). Taken together, these findings demonstrate that MφMB-Au displays excellent *in vivo* biocompatibility without inducing detectable systemic toxicity or immune responses.

4. Conclusions

In this study, we developed an engineered living-cell drug delivery system capable of site-specific drug accumulation and controlled release within AS plaques. Notably, this targeted delivery process can be dynamically monitored in real time and over extended periods (up to 24 hours) *via* dual-modality US/PA imaging. Specifically, as progresses, MφMB-Au leverages its intrinsic inflammation-homing capacity to migrate and accumulate at inflamed plaque regions. Upon ultrasound irradiation, the AuNPs are released, further promoting the polarization of MφMB-Au toward an anti-inflammatory M2 macrophage phenotype. In an AS mouse model, MφMB-Au demonstrated robust plaque-specific accumulation and significantly attenuated disease progression. Therapeutic intervention also led to an increased (Treg + M2)/(Th1 + Th2 + M1) ratio, suggesting an improved systemic inflammatory profile. Moreover, long-term administration of MφMB-Au resulted in no observable adverse effects, confirming its favourable biosafety. Overall, this dual-modality imaging-compatible, engineered macrophage-based delivery platform has promising potential for the treatment of AS.

Author contributions

Conceptualization: Yingying Liu, Jinfeng Xu and Liqiang Zhou; data curation: Wei Zeng, Yuhang Mao, Weiming Fang and Yalan Huang; formal analysis: Wei Zeng; funding acquisition: Jinfeng Xu, Yingying Liu and Liqiang Zhou; investigation: Wei Zeng, Yuhang Mao, Yan Lin, Leilei Wu, Yuanyuan Sheng and Xiaoxuan Lin; methodology: Yingying Liu; project administration: Yingying Liu and Liqiang Zhou; resources: Wei Zeng, Weiming Fang, Yalan Huang, Anqi Chen, Zhengan Huang, Jiayu Ye, Yanbin Guo, Guanxi Wen and Jian Zeng; software: Wei Zeng and Weiming Fang; supervision: Yingying Liu; validation, Wei Zeng, Jinfeng Xu and Yingying Liu; visualization: Wei Zeng, Weiming Fang and Yalan Huang; writing – original draft: Wei Zeng; and writing – review & editing: Yingying Liu and Liqiang Zhou. All authors have read and agreed to the published version of the manuscript.

Conflicts of interest

The authors declare that they have no known competing financial interests or personal relationships that could have appeared to influence the work reported in this paper.

Data availability

The data supporting this article have been included as part of the supplementary information (SI). Supplementary information is available. See DOI: https://doi.org/10.1039/d5mh01682g.

Acknowledgements

This work was financially supported by the National Natural Science Foundation of China (82102041 and 82302369), the Shenzhen Medical Research Fund (A2503015), the Shenzhen Medical Research Special Project clinical multi-center study (C2405001), the Project of International cooperative research of the Science and Technology Commission of Shenzhen City (GJHZ20210705142205017), the Science and Technology Development Fund, Macau SAR (File No. 0032/2023/ITP1) and Shenzhen Science and Technology Program (JCYJ20250604142033004).

References

1 S. Y. Chong, X. Wang, L. van Bloois, C. Huang, N. S. Syeda, S. Zhang, H. J. Ting, V. Nair, Y. Lin, C. K. L. Lou, A. A. Benetti, X. Yu, N. J. Y. Lim, M. S. Tan, H. Y. Lim, S. Y. Lim, C. H. Thiam, W. D. Looi, O. Zharkova, N. W. S. Chew, C. H. Ng, G. K. Bonney, M. Muthiah, X. Chen, G. Pastorin, A. M. Richards, V. Angeli, G. Storm and J. W. Wang, *J. Controlled Release*, 2023, **360**, 344–364.
2 K. Zhang, T. Wang, X. Huang, P. Wu, L. Shen, Y. Yang, W. Wan, S. Sun and Z. Zhang, *Ultrason. Sonochem.*, 2025, **114**, 107270.
3 P. Libby, J. E. Buring, L. Badimon, G. K. Hansson, J. Deanfield, M. S. Bittencourt, L. Tokgözoğlu and E. F. Lewis, *Nat. Rev. Dis. Primers*, 2019, **5**, 56.
4 R. Virmani, A. P. Burke, A. Farb and F. D. Kolodgie, *J. Am. Coll. Cardiol.*, 2006, **47**, C13–C18.
5 M. Banach, Ž. Reiner, S. Surma, G. Bajraktari, A. Bielecka-Dabrowa, M. Bunc, I. Bytyçi, R. Ceska, A. F. G. Cicero, D. Dudek, K. Dyrbuś, J. Fedacko, Z. Fras, D. Gaita, D. Gavish, M. Gierlotka, R. Gil, I. Gouni-Berthold, P. Jankowski, Z. Járai, J. Jóźwiak, N. Katsiki, G. Latkovskis, S. L. Magda, E. Margetic, R. Margoczy, O. Mitchenko, A. Durak-Nalbantic, P. Ostadal, G. Paragh, Z. Petrulioniene, F. Paneni, I. Pećin, D. Pella, A. Postadzhiyan, A. P. Stoian, M. Trbusic, C. A. Udroiu, M. Viigimaa, D. Vinereanu, C. Vlachopoulos, M. Vrablik, D. Vulic and P. E. Penson, *Drugs*, 2024, **84**, 1541–1577.
6 P. M. Ridker, B. M. Everett, T. Thuren, J. G. MacFadyen, W. H. Chang, C. Ballantyne, F. Fonseca, J. Nicolau, W. Koenig, S. D. Anker, J. J. P. Kastelein, J. H. Cornel, P. Pais, D. Pella, J. Genest, R. Cifkova, A. Lorenzatti, T. Forster, Z. Kobalava, L. Vida-Simiti, M. Flather, H. Shimokawa, H. Ogawa, M. Dellborg, P. R. F. Rossi, R. P. T. Troquay, P. Libby and R. J. Glynn, *N. Engl. J. Med.*, 2017, **377**, 1119–1131.
7 W. Herrington, B. Lacey, P. Sherliker, J. Armitage and S. Lewington, *Circ. Res.*, 2016, **118**, 535–546.

 This journal is © The Royal Society of Chemistry 2025

Open Access Article. Published on 23 December 2025. Downloaded on 1/24/2026 10:53:48 PM. This article is licensed under a Creative Commons Attribution-NonCommercial 3.0 Unported Licence.

8 S. J. Head, M. Milojevic, J. Daemen, J. M. Ahn, E. Boersma, E. H. Christiansen, M. J. Domanski, M. E. Farkouh, M. Flather, V. Fuster, M. A. Hlatky, N. R. Holm, W. A. Hueb, M. Kamalesh, Y. H. Kim, T. Mäkikallio, F. W. Mohr, G. Papageorgiou, S. J. Park, A. E. Rodriguez, J. F. Sabik, 3rd, R. H. Stables, G. W. Stone, P. W. Serruys and A. P. Kappetein, *Lancet*, 2018, **391**, 939–948.
9 M. D. Müller, P. Lyrer, M. M. Brown and L. H. Bonati, *Cochrane Database Syst. Rev.*, 2020, **2**, Cd000515.
10 W. T. Ma, F. Gao, K. Gu and D. K. Chen, *Front. Immunol.*, 2019, **10**, 1140.
11 L. Duong, H. G. Radley, B. Lee, D. E. Dye, F. J. Pixley, M. D. Grounds, D. J. Nelson and C. Jackaman, *Immun. Ageing*, 2021, **18**, 4.
12 X. Li, R. Liu, X. Su, Y. Pan, X. Han, C. Shao and Y. Shi, *Mol. Cancer*, 2019, **18**, 177.
13 G. Bajpai, C. Schneider, N. Wong, A. Bredemeyer, M. Hulsmans, M. Nahrendorf, S. Epelman, D. Kreisel, Y. Liu, A. Itoh, T. S. Shankar, C. H. Selzman, S. G. Drakos and K. J. Lavine, *Nat. Med.*, 2018, **24**, 1234–1245.
14 L. Song, J. Zhang, D. Ma, Y. Fan, R. Lai, W. Tian, Z. Zhang, J. Ju and H. Xu, *Front. Immunol.*, 2022, **13**, 910444.
15 L. Zhang, J. Li, Y. Kou, L. Shen, H. Wang, Y. Wang, R. Ma, T. Wu, X. Yang, Y. Gu and L. Yi, *Front. Immunol.*, 2024, **15**, 1490387.
16 F. O. Martinez and S. Gordon, *F1000Prime Rep.*, 2014, **6**, 13.
17 J. Zhao, Z. Chen, S. Liu, P. Li, S. Yu, D. Ling and F. Li, *BMEMat*, 2024, **2**, e12066.
18 D. G. DeNardo and B. Ruffell, *Nat. Rev. Immunol.*, 2019, **19**, 369–382.
19 J. Yao, K. Sterling, Z. Wang, Y. Zhang and W. Song, *Signal Transduction Targeted Ther.*, 2024, **9**, 10.
20 T. J. Barrett, *Arterioscler., Thromb., Vasc. Biol.*, 2020, **40**, 20–33.
21 Y. Bi, J. Chen, F. Hu, J. Liu, M. Li and L. Zhao, *Neural Plast.*, 2019, **2019**, 6724903.
22 S. Gordon and F. O. Martinez, *Immunity*, 2010, **32**, 593–604.
23 L. Xu, J. Qiu, Q. Ren, D. Wang, A. Guo, L. Wang, K. Hou, R. Wang and Y. Liu, *Mater. Today Bio*, 2025, **32**, 101653.
24 G. Hu, M. Guo, J. Xu, F. Wu, J. Fan, Q. Huang, G. Yang, Z. Lv, X. Wang and Y. Jin, *Front. Immunol.*, 2019, **10**, 1998.
25 W. Huang, R. Chen, Y. Peng, F. Duan, Y. Huang, W. Guo, X. Chen and L. Nie, *ACS Nano*, 2019, **13**, 9561–9570.
26 W. Chen, F. Zhang, Y. Ju, J. Hong and Y. Ding, *Adv. Healthcare Mater.*, 2021, **10**, e2000818.
27 Y. Xie, Y. Xianyu, N. Wang, Z. Yan, Y. Liu, K. Zhu, N. S. Hatzakis and X. Jiang, *Adv. Funct. Mater.*, 2018, **28**, 1702026.
28 Y. Tao, H. F. Chan, B. Shi, M. Li and K. W. Leong, *Adv. Funct. Mater.*, 2020, **30**, 2005029.
29 Y.-S. Chen, D. Yeager and S. Y. Emelianov, in *Cancer Theranostics*, ed. X. Chen and S. Wong, Academic Press, Oxford, 2014, pp. 139–158, DOI: 10.1016/B978-0-12-407722-5.00009-8.
30 Y. Sun, X. Yu, X. Wang, K. Yuan, G. Wang, L. Hu, G. Zhang, W. Pei, L. Wang, C. Sun and P. Yang, *Acta Pharm. Sin. B*, 2023, **13**, 3583–3597.
31 L. Sun, J. E. Zhou, T. Luo, J. Wang, L. Kang, Y. Wang, S. Luo, Z. Wang, Z. Zhou, J. Zhu, J. Yu, L. Yu and Z. Yan, *Adv. Mater.*, 2022, **34**, e2109969.
32 Y. Huang, Z. Guan, X. Dai, Y. Shen, Q. Wei, L. Ren, J. Jiang, Z. Xiao, Y. Jiang, D. Liu, Z. Huang, X. Xu, Y. Luo and C. Zhao, *Nat. Commun.*, 2021, **12**, 4310.
33 J. Xue, Z. Zhao, L. Zhang, L. Xue, S. Shen, Y. Wen, Z. Wei, L. Wang, L. Kong, H. Sun, Q. Ping, R. Mo and C. Zhang, *Nat. Nanotechnol.*, 2017, **12**, 692–700.
34 L. Zhou, Y. Chen, D. Xie, K. Li, X. Cui, C. F. Dietrich, A. K. Nüssler and X. Zhang, *BMEMat*, 2024, **2**, e12079.
35 M. M. Salem-Bekhit, A. M. E. Youssof, F. K. Alanazi, F. S. Aleanizy, A. Abdulaziz, E. I. Taha and A. Amara, *Pharmaceutics*, 2021, **13**, 1984.
36 B. D. Kevadiya, B. M. Ottemann, M. B. Thomas, I. Mukadam, S. Nigam, J. McMillan, S. Gorantla, T. K. Bronich, B. Edagwa and H. E. Gendelman, *Adv. Drug Delivery Rev.*, 2019, **148**, 252–289.
37 N. Gautam, J. M. McMillan, D. Kumar, A. N. Bade, Q. Pan, T. A. Kulkarni, W. Li, B. Sillman, N. A. Smith, B. L. D. Shetty, A. Szlachetka, B. J. Edagwa, H. E. Gendelman and Y. Alnouti, *Nat. Commun.*, 2021, **12**, 3453.
38 W. Chen, M. Schilperoort, Y. Cao, J. Shi, I. Tabas and W. Tao, *Nat. Rev. Cardiol.*, 2022, **19**, 228–249.
39 M. Zhu, L. Du, R. Zhao, H. Y. Wang, Y. Zhao, G. Nie and R. F. Wang, *ACS Nano*, 2020, **14**, 3703–3717.
40 W. Zeng, Z. Huang, Y. Huang, K. Xiong, Y. Sheng, X. Lin, X. Zhong, J. Ye, Y. Guo, G. Arkin, J. Xu, H. Fei and Y. Liu, *Mater. Today Bio*, 2025, **32**, 101675.
41 X. Bai, D. Chen, Y. Dai, S. Liang, B. Song, J. Guo, B. Dai, D. Zhang and L. Feng, *Nanomedicine*, 2021, **38**, 102457.
42 B. Ibrahim, T. H. Akere, S. Chakraborty, E. Valsami-Jones and H. Ali-Boucetta, *Pharmaceutics*, 2023, **15**, 432.
43 Q. Xia, J. Huang, Q. Feng, X. Chen, X. Liu, X. Li, T. Zhang, S. Xiao, H. Li, Z. Zhong and K. Xiao, *Int. J. Nanomed.*, 2019, **14**, 6957–6970.
44 K. P. Steckiewicz, E. Barcinska, A. Malankowska, A. Zauszkiewicz-Pawlak, G. Nowaczyk, A. Zaleska-Medynska and I. Inkielewicz-Stepniak, *J. Mater. Sci.: Mater. Med.*, 2019, **30**, 22.
45 C. Wang, S. Wang, D. D. Kang and Y. Dong, *BMEMat*, 2023, **1**, e12039.
46 E. Liu, D. Marin, P. Banerjee, H. A. Macapinlac, P. Thompson, R. Basar, L. Nassif Kerbauy, B. Overman, P. Thall, M. Kaplan, V. Nandivada, I. Kaur, A. Nunez Cortes, K. Cao, M. Daher, C. Hosing, E. N. Cohen, P. Kebriaei, R. Mehta, S. Neelapu, Y. Nieto, M. Wang, W. Wierda, M. Keating, R. Champlin, E. J. Shpall and K. Rezvani, *N. Engl. J. Med.*, 2020, **382**, 545–553.
47 T. L. Roth, C. Puig-Saus, R. Yu, E. Shifrut, J. Carnevale, P. J. Li, J. Hiatt, J. Saco, P. Krystofinski, H. Li, V. Tobin, D. N. Nguyen, M. R. Lee, A. L. Putnam, A. L. Ferris, J. W. Chen, J. N. Schickel, L. Pellerin, D. Carmody, G. Alkorta-Aranburu, D. Del Gaudio, H. Matsumoto, M. Morell, Y. Mao, M. Cho, R. M. Quadros, C. B. Gurumurthy, B. Smith, M. Haugwitz, S. H. Hughes, J. S. Weissman, K. Schumann, J. H. Esensten, A. P. May, A. Ashworth, G. M. Kupfer,

Open Access Article. Published on 23 December 2025. Downloaded on 1/24/2026 10:53:48 PM.
This article is licensed under a Creative Commons Attribution-NonCommercial 3.0 Unported Licence.

S. A. W. Greeley, R. Bacchetta, E. Meffre, M. G. Roncarolo, N. Romberg, K. C. Herold, A. Ribas, M. D. Leonetti and A. Marson, *Nature*, 2018, **559**, 405–409.

48 M. A. Hassan, K. Al-Sakkaf, M. R. Shait Mohammed, A. Dallol, J. Al-Maghrabi, A. Aldahlawi, S. Ashoor, M. Maamra, J. Ragoussis, W. Wu, M. I. Khan, A. L. Al-Malki and H. Choudhry, *Front. Oncol.*, 2020, **10**, 804.

49 Y. Cui, J. Chen, Z. Zhang, H. Shi, W. Sun and Q. Yi, *J. Transl. Med.*, 2023, **21**, 892.

50 X. Qiao, Z. Hu, F. Xiong, Y. Yang, C. Peng, D. Wang and X. Li, *Lipids Health Dis.*, 2023, **22**, 45.

51 P. K. Morgan, K. Huynh, G. Pernes, P. M. Miotto, N. A. Mellett, C. Giles, P. J. Meikle, A. J. Murphy and G. I. Lancaster, *J. Biol. Chem.*, 2021, **297**, 101341.

52 J. Qiu, Z. Wang, Y. Yu, Y. Zheng, M. Li and C. Lin, *Int. Immunopharmacol.*, 2024, **132**, 111940.

53 J. Cai, Z. Ye, Y. Hu, L. Ye, L. Gao, Y. Wang, Q. Sun, S. Tong, S. Zhang, L. Wu, J. Yang and Q. Chen, *Cell Death Dis.*, 2023, **14**, 211.

54 A. A. Belew, S. H. Gebre, M. A. Assege, D. S. Meshesha and M. T. Ayana, *Results Chem.*, 2025, **18**, 102859.

55 X. Liao, G. Gong, M. Dai, Z. Xiang, J. Pan, X. He, J. Shang, A. M. Blocki, Z. Zhao, C. W. T. Shields and J. Guo, *Adv. Sci.*, 2023, **10**, e2207488.

56 J. L. Witztum and A. H. Lichtman, *Annu. Rev. Pathol.:Mech. Dis.*, 2014, **9**, 73–102.

57 M. Sharma, M. P. Schlegel, M. S. Afonso, E. J. Brown, K. Rahman, A. Weinstock, B. E. Sansbury, E. M. Corr, C. van Solingen, G. J. Koelwyn, L. C. Shanley, L. Beckett, D. Peled, J. J. Lafaille, M. Spite, P. Loke, E. A. Fisher and K. J. Moore, *Circ. Res.*, 2020, **127**, 335–353.

58 C. Buono, C. J. Binder, G. Stavrakis, J. L. Witztum, L. H. Glimcher and A. H. Lichtman, *Proc. Natl. Acad. Sci. U. S. A.*, 2005, **102**, 1596–1601.

59 C. Buono, C. E. Come, G. Stavrakis, G. F. Maguire, P. W. Connelly and A. H. Lichtman, *Arterioscler., Thromb., Vasc. Biol.*, 2003, **23**, 454–460.

 This journal is © The Royal Society of Chemistry 2025